GW in the Gaussian and plane waves scheme with application to linear acenes

Wilhelm, Jan ; Del Ben, Mauro ; Hutter, Jürg

Abstract: We present an implementation of G0W0 and eigenvalue-self-consistent GW (evGW) in the Gaussian and plane waves scheme for molecules. We calculate the correlation self-energy for imaginary frequencies employing the resolution of the identity. The correlation self-energy for real frequencies is then evaluated by analytic continuation. This technique allows an efficient parallel implementation and application to systems with several hundreds of atoms. Various benchmark calculations are presented. In particular, the convergence with respect to the most important numerical parameters is assessed for the benzene molecule. Comparisons with respect to other G0W0 implementations are reported for a set of molecules, while the performance of the method has been measured for water clusters containing up to 480 atoms in a cc-TZVP basis. Additionally, G0W0 has been applied for studying the influence of the ligands on the gap of small CdSe nanoparticles. evGW has been employed to calculate the HOMO–LUMO gaps of linear acenes, linear chains formed of connected benzene rings. Distinct differences between the closed and the open-shell (broken-symmetry) evGW HOMO–LUMO gaps for long acenes are found. In future experiments, a comparison of measured HOMO–LUMO gaps and our calculated evGW values may be helpful to determine the electronic ground state of long acenes.

DOI: https://doi.org/10.1021/acs.jctc.6b00380

GW in the Gaussian and plane waves scheme with application to linear acenes

Jan Wilhelm,[*,†] Mauro Del Ben,[‡] and Jürg Hutter[†]

†*Department of Chemistry and National Centre for Computational Design and Discovery of Novel Materials (MARVEL), University of Zurich, 8057 Zurich, Switzerland*

‡*Computational Research Division, Lawrence Berkeley National Laboratory, Berkeley, California 94720, United States*

E-mail: jan.wilhelm@chem.uzh.ch

Abstract

We present an implementation of G_0W_0 and eigenvalue-self-consistent GW (evGW) in the Gaussian and plane waves scheme for molecules. Technically, we calculate the correlation self-energy for imaginary frequencies employing the resolution of the identity. The correlation self-energy for real frequencies is then evaluated by analytic continuation. This technique allows an efficient parallel implementation and application to systems with several hundreds of atoms. Various benchmark calculations are presented. In particular, the convergence with respect to the most important numerical parameters is assessed for the benzene molecule. Comparisons with respect to other G_0W_0 implementations are reported for a set of molecules, while the performance of the method has been measured for water clusters containing up to 480 atoms in a cc-TZVP basis. Additionally, G_0W_0 has been applied for studying the influence of the ligands on the gap of small CdSe nanoparticles. evGW has been employed to calculate the HOMO-LUMO gaps of linear acenes, linear chains formed of connected benzene rings. Distinct differences between the closed and the open-shell (broken-symmetry) evGW

HOMO-LUMO gaps for long acenes are found. In future experiments, a comparison of measured HOMO-LUMO gaps and our calculated evGW values may be helpful to determine the electronic groundstate of long acenes.

1 Introduction

In recent years, GW with localized basis sets has emerged as an accurate method for the calculation of quasiparticle energies of molecules[1–19]. Additionally, in combination with the Bethe-Salpeter equation, GW is a promising method for computing molecular electronic excitations with high accuracy[7,20–25]. Most of the traditional GW implementations employ a plane-wave (PW) or augmented plane-wave (APW) basis[26–44]. While the main field of application of PW and APW GW is still the condensed phase, they have also been employed recently to calculate quasiparticle levels of molecules[45–48]. When treating molecules, the main advantage of a localized basis compared to PWs is the reduced number of basis functions required to represent the Hamiltonian and thus the wavefunctions. The number of PWs can be a factor 100-1000 larger compared to that of a localized basis,[49] mainly due to the need of a large supercell in the former method in order to decouple the periodic images. On the other hand, the generation of a localized basis that provides systematic convergence is much harder to be obtained and the convergence of the GW quasiparticle energies with respect to the basis parameters is still under investigation.[2,9,12,14]

The computational effort of G_0W_0 is quickly growing for increasing system size N with a scaling $\mathcal{O}(N^4)$ for state-of-the-art implementations[1]. As consequence, an efficient implementation for high-performance computing is needed to study large systems with G_0W_0[27,46]. As basis of our G_0W_0 implementation in the Gaussian and plane waves scheme[50] in CP2K[51,52], we employ the previous efficient implementation of wavefunction correlation methods[53–56] which enabled large-scale molecular-dynamics and Monte Carlo simulations based on second order Møller-Plesset (MP2) and random phase approximation (RPA) total energies[57–59]. We use the G_0W_0 framework in the resolution-of-the-identity approach as elaborated by Ren *et*

al.[1] Our G_0W_0 methodology can be applied to systems containing hundreds of atoms. As starting point for G_0W_0, a wide range of local, semilocal, hybrid and range-separated hybrid functionals can be employed[60]. In agreement with the literature[1,2,14,21,22,46,61–63], we find that the PBE0[64] and the tuned CAM-B3LYP[65] starting points perform remarkably well for molecules with an average deviation of $0.1-0.2\,\mathrm{eV}$ between the computed G_0W_0-HOMO energy and the experimental vertical ionization potential[66]. Moreover, our G_0W_0 and evGW implementation can treat systems with unpaired electrons.

We apply our GW implementation to compute the HOMO-LUMO gap of linear acenes, molecules consisting of repeating units of benzene rings. This application is motivated by a recent study by Korytár *et al.*[67] indicating that the HOMO-LUMO gaps of acenes may not decay monotonously with increasing number of benzene rings, but can oscillate. The reason is the presence of a level crossing in the one-dimensional band structure of polyacene[68] which is shifted from the Γ-point. Such HOMO-LUMO gap oscillations are well-known in carbon nanotubes[69,70] and armchair graphene nanoribbons[71–74] due to the presence of the Dirac cone in the band structure of graphene[75]. Remarkably, the HOMO-LUMO gap oscillations in acenes on the level of closed-shell PBE[76] have not been reported before Ref. 67 despite of the intensive research on the electronic groundstate properties of acenes[77–84], which is driven by organic electronics[85–89] and photovoltaics[90–94]. In Ref. 67, G_0W_0 HOMO-LUMO gaps have been presented up to tetracene. We report G_0W_0 and eigenvalue-selfconsistent GW[6,7] calculations of the HOMO-LUMO gap up to 11-acene.

The manuscript is organized as follows: First, we introduce the GW methodology of our implementation (Sec. 2). In Sec. 3, we perform extensive benchmark calculations with our implementation: the convergence of a wide range of numerical parameters is illustratively tested for benzene. We report about execution times, system size scaling and the parallel speedup measured for water clusters containing up to 160 molecules. Also, G_0W_0-HOMO energies of molecules and G_0W_0 gaps of CdSe nanoclusters are reported. In Sec. 4, we apply eigenvalue-self-consistent GW to predict the HOMO-LUMO gap of linear acenes.

2 Theory and implementation

In this section, the theoretical and computational framework of the G_0W_0 implementation is briefly presented. In Sec. 2.1, we describe the evaluation of the quasiparticle energies starting from the precomputed frequency-dependent correlation-self-energy $\Sigma^{\mathrm{c}}(\omega)$.[1,2] The resolution-of-the-identity (RI) approximation for four-center two electron repulsion integrals (ERIs) is introduced in Sec. 2.2.[54] In Sec. 2.3, we apply RI to G_0W_0 and we give the working expressions as employed in the implementation.[1,54]

The following index notation has been adopted: μ, ν, λ refer to Gaussian functions ϕ of the primary basis, n, m, k, l refer to general molecular orbitals (MOs) ψ, i to an occupied MO, a to a virtual one and P, Q to auxiliary RI Gaussian basis functions φ.

2.1 Starting point and quasiparticle energies

For G_0W_0, we start from a self-consistent generalized Kohn-Sham (GKS) DFT[95] calculation, including hybrid functionals and Hartree-Fock (HF)[96]. The total energy of a many-electron system in GKS-DFT is obtained by solving the eigenvalue problem

$$h^0\psi_n(\mathbf{r}) + \int d\mathbf{r}'\, v^{\mathrm{xc}}(\mathbf{r},\mathbf{r}')\psi_n(\mathbf{r}') = \varepsilon_n\psi_n(\mathbf{r})\,. \tag{1}$$

h^0 contains the external and the Hartree potential as well as the kinetic energy. $v^{\mathrm{xc}}(\mathbf{r},\mathbf{r}')$ denotes the exchange-correlation potential which is local for most non-hybrid density functional approximations, $v^{\mathrm{xc}}(\mathbf{r},\mathbf{r}') = \delta(\mathbf{r},\mathbf{r}')v^{\mathrm{xc}}_{\mathrm{KS}}(\mathbf{r})$. In HF, exact exchange[97–99]

$$\Sigma^{\mathrm{x}}(\mathbf{r},\mathbf{r}') = -\sum_{i}^{\mathrm{occ}} \psi_i(\mathbf{r})\psi_i(\mathbf{r}')v(\mathbf{r},\mathbf{r}') \tag{2}$$

is the only term included in $v^{\mathrm{xc}}(\mathbf{r},\mathbf{r}')$, where $v(\mathbf{r},\mathbf{r}') = 1/|\mathbf{r}-\mathbf{r}'|$ denotes the bare Coulomb interaction. In this case the potential is fully non-local and no correlation effects are accounted. Note that the spin variable has been dropped for convenience.

In the following, we briefly introduce the G_0W_0 method giving the equation to compute the quasiparticle energies $\varepsilon_n^{G_0W_0}$. For a concise introduction into quasiparticles and the *GW* method in the Green's function framework, we refer to the work of Hüser *et al.*[45] By construction, the GKS-DFT MOs $\psi_n(\mathbf{r})$ and their corresponding eigenvalues ε_n are auxiliary quantities for computing the total energy of the many-body problem. In contrast, the poles of the Green's function correspond to vertical electron addition or removal energies and consequently, these poles are interpreted as quasiparticle energies.[45] In G_0W_0, the MOs from GKS-DFT serve as quasiparticle wavefunctions and only their quasiparticle energies (poles of the Green's function) are computed by means of G_0W_0:

$$\varepsilon_n^{G_0W_0} = \varepsilon_n + Z_n(n|\Sigma^{\mathrm{x}} + \mathrm{Re}\,\Sigma^{\mathrm{c}}(\varepsilon_n) - v^{\mathrm{xc}}|n)\,, \tag{3}$$

where $\Sigma^{\mathrm{c}}(\varepsilon)$ stands for the G_0W_0 correlation self-energy which is calculated according to the algorithm described in the following sections. The renormalization factor Z_n,

$$Z_n = \left(1 - \partial(n|\mathrm{Re}\,\Sigma^{\mathrm{c}}(\omega)|n)/\partial\omega|_{\omega=\varepsilon_n}\right)^{-1}\,, \tag{4}$$

accounts for the linearized energy-dependence of $\Sigma^{\mathrm{c}}(\omega)$.[2]

2.2 RI approximation

The four-center electron repulsion integrals (ERIs) are of central importance for calculating the correlation self-energy $\Sigma^{\mathrm{c}}(\varepsilon)$ in the G_0W_0 approximation. These integrals, in Mulliken notation, are defined as

$$(nm|kl) := \int d\mathbf{r}\,d\mathbf{r}'\,\psi_n(\mathbf{r}')\psi_m(\mathbf{r}')\psi_k(\mathbf{r})\psi_l(\mathbf{r})v(\mathbf{r},\mathbf{r}') \tag{5}$$

where $v(\mathbf{r},\mathbf{r}')=1/|\mathbf{r}-\mathbf{r}'|$ is the Coulomb interaction. Within the RI approximation[100,101] based on the Coulomb metric[102], these integrals are factorized to

$$(nm|kl)_{\mathrm{RI}} = \sum_{PQ}(nm|P)V^{-1}_{PQ}(Q|kl)\,. \tag{6}$$

Here, V^{-1}_{PQ} is the inverse of the Coulomb matrix V_{PQ}:

$$V_{PQ} \equiv (P|Q) = \int d\mathbf{r}\,d\mathbf{r}'\varphi_P(\mathbf{r}')\varphi_Q(\mathbf{r})v(\mathbf{r},\mathbf{r}')\,. \tag{7}$$

The matrix elements $(nm|P)$ are given by

$$(nm|P) = \sum_{\mu\nu} C_{\mu n}C_{\nu m}(\mu\nu|P)\,, \tag{8}$$

$$(\mu\nu|P) = \int d\mathbf{r}\,d\mathbf{r}'\phi_\mu(\mathbf{r}')\phi_\nu(\mathbf{r}')\varphi_P(\mathbf{r})v(\mathbf{r},\mathbf{r}') \tag{9}$$

where the $C_{\lambda k}$ are the elements of the MO coefficient matrix obtained as solution of the KS equations.

The RI-basis functions P,Q are Gaussian functions, which are local for gas phase systems and periodically repeated for the condensed phase. The two- and three-center ERIs are computed by direct integration between the Gaussian basis functions [bra in Eq. (7) and (9)] and the electrostatic potential associated to auxiliary RI Gaussian basis functions [ket in Eq. (7) and (9)]. The electrostatic potential is obtained in a plane wave basis set after solving the Poisson equation in Fourier space. The advantage of this method is that, for each electrostatic potential, the evaluation of the matrix elements of Eq. (9) is obtained in linear scaling time, since only integrals over overlapping basis function product $\phi_\mu(\mathbf{r}')\phi_\nu(\mathbf{r}')$ need to be evaluated. Additionally, due to the introduction of an auxiliary PW basis for the expansion of the electrostatic densities, periodic boundary conditions can be included straightforwardly. On the other hand, pseudopotentials have to be employed in order to

remove core states and to provide smooth densities. For more details, we refer to Ref. 54.

The main advantage of the RI approximation [Eq. (6)] is that four center electron repulsion integrals of the type $(nm|kl)$ are computed from three and two center ERIs. This allows to strongly reduce the storage requirement as well as the computational effort for the integral evaluation and subsequent matrix operations without significant loss of accuracy.[101,103]

Since the Coulomb matrix V_{PQ} is positive definite, the calculation of V_{PQ}^{-1} can be efficiently performed by a Cholesky decomposition of V_{PQ},

$$V_{PQ} = \sum_R L_{PR} L_{RQ}^T \tag{10}$$

followed by the efficient inversion of the triangular matrix $\mathbf{L}$ such that

$$V_{PQ}^{-1} = \sum_R L_{PR}^{-T} L_{RQ}^{-1} \,. \tag{11}$$

In this way, the factorization of the $(nm|kl)$ ERIs can be expressed in a compact form as

$$(nm|kl)_{\mathrm{RI}} = \sum_P B_P^{nm} B_P^{kl} \,, \tag{12}$$

where $\mathbf{B}$ is given by

$$B_P^{nm} = \sum_R (nm|R) L_{PR}^{-1} \,. \tag{13}$$

2.3 G_0W_0 self-energy

In the GW approximation[104], the G_0W_0 self-energy $\Sigma = \Sigma^{\mathrm{x}} + \Sigma^{\mathrm{c}}$ for an imaginary frequency $i\omega$ is given by[1]

$$\begin{aligned} \Sigma(\mathbf{r}, \mathbf{r}', i\omega) = -\frac{1}{2\pi} \int_{-\infty}^{\infty} d\omega' G_0(\mathbf{r}, \mathbf{r}', i\omega - i\omega') \\ \times W_0(\mathbf{r}, \mathbf{r}', i\omega') \end{aligned} \tag{14}$$

where $G_0(\mathbf{r},\mathbf{r}',i\omega)$ is the Green's function of the KS reference system [Eq. (1)],

$$G_0(\mathbf{r},\mathbf{r}',i\omega) = \sum_m \frac{\psi_m(\mathbf{r}')\psi_m(\mathbf{r})}{i\omega + \varepsilon_\mathrm{F} - \varepsilon_m}\,, \tag{15}$$

and $W_0(\mathbf{r},\mathbf{r}',i\omega)$ the screened Coulomb interaction,

$$W_0(\mathbf{r},\mathbf{r}',i\omega) = \int d\mathbf{r}''\epsilon^{-1}(\mathbf{r},\mathbf{r}'',i\omega)v(\mathbf{r}'',\mathbf{r}')\,. \tag{16}$$

The dielectric function $\epsilon(\mathbf{r},\mathbf{r}',i\omega)$ is defined as

$$\epsilon(\mathbf{r},\mathbf{r}',i\omega) = \delta(\mathbf{r},\mathbf{r}') - \int d\mathbf{r}''v(\mathbf{r},\mathbf{r}'')\chi(\mathbf{r}'',\mathbf{r}',i\omega)\,. \tag{17}$$

With $(1-x)^{-1} = 1 + x + x^2 + \ldots$ for $|x| < 1$, we write

$$\epsilon^{-1}(\mathbf{r},\mathbf{r}',i\omega) = \delta(\mathbf{r},\mathbf{r}') + \int d\mathbf{r}''v(\mathbf{r},\mathbf{r}'')\chi(\mathbf{r}'',\mathbf{r}',i\omega) + \ldots \tag{18}$$

where the density response $\chi(\mathbf{r},\mathbf{r}',i\omega)$ is given by

$$\begin{aligned}\chi(\mathbf{r},\mathbf{r}',i\omega) = 2\sum_i^{\mathrm{occ}}\sum_a^{\mathrm{virt}} &\psi_a(\mathbf{r}')\psi_i(\mathbf{r}')\psi_i(\mathbf{r})\psi_a(\mathbf{r}) \\ &\times \frac{\varepsilon_i - \varepsilon_a}{\omega^2 + (\varepsilon_i - \varepsilon_a)^2}\,.\end{aligned} \tag{19}$$

In order to employ Eq. (3), we calculate the (n,n)-diagonal matrix element of $\Sigma(i\omega)$,

$$\Sigma_n(i\omega) \equiv (n|\Sigma(i\omega)|n) = \int d\mathbf{r}d\mathbf{r}'\psi_n(\mathbf{r}')\psi_n(\mathbf{r})\Sigma(\mathbf{r},\mathbf{r}',i\omega) \tag{20}$$

for considered quasiparticle state n and for a given set of $i\omega$ grid points. By considering N_aux RI-auxiliary Gaussian functions P and Q, inserting the Eqs. (14) – (16), (18), (19) and then

Eq. (6) and (12) into Eq. (20), we obtain[1]

$$\begin{aligned}\Sigma_n(i\omega) = &-\frac{1}{2\pi}\sum_m \int_{-\infty}^{\infty} d\omega' \frac{1}{i(\omega-\omega')+\varepsilon_\mathrm{F}-\varepsilon_m} \\ &\times \sum_{PQ} B_P^{nm}\left[1-\Pi(i\omega')\right]^{-1}_{PQ} B_Q^{mn}\,,\end{aligned} \tag{21}$$

where $\Pi_{PQ}(i\omega)$ is the $N_\mathrm{aux}\times N_\mathrm{aux}$ matrix representation of the density response function,

$$\Pi_{PQ}(i\omega) = 2\sum_{ia} B_P^{ia}\frac{\varepsilon_i-\varepsilon_a}{\omega^2+(\varepsilon_i-\varepsilon_a)^2} B_Q^{ia}\,. \tag{22}$$

For numerical stability and to avoid the RI-approximation for Σ_n^x, we calculate the exact exchange self-energy by means of Eq. (2):

$$\Sigma_n^\mathrm{x} := (n|\Sigma^\mathrm{x}|n) = -\sum_i^\mathrm{occ}(ni|in)\,. \tag{23}$$

The exchange self-energy [Eq. (23)] is subtracted from the total self-energy to obtain the correlation part. Similarly to Eq. (21), we get[13]

$$\begin{aligned}\Sigma_n^\mathrm{c}(i\omega) = &-\frac{1}{2\pi}\sum_m \int_{-\infty}^{\infty} d\omega' \frac{1}{i(\omega-\omega')+\varepsilon_\mathrm{F}-\varepsilon_m} \\ &\times \sum_{PQ} B_P^{nm}\left[\left[1-\Pi(i\omega')\right]^{-1}_{PQ}-\delta_{PQ}\right] B_Q^{mn}\,.\end{aligned} \tag{24}$$

The integration over ω' is computed employing a Clenshaw-Curtis grid[105] as proposed by Eshuis *et al.*[106] We employ the same grid to evaluate $\Sigma_n^\mathrm{c}(i\omega)$.

To evaluate Eq. (3), we obtain the real-frequency self-energy by means of analytic continuation[107,108] which has been proven to be accurate[1,12,13,34,109,110]. In this approach, $\Sigma_n^\mathrm{c}(i\omega)$ from Eq. (24) is fit to a two-pole model P_n for every quasiparticle state n ($N_\mathrm{poles}=2$):

$$\Sigma_n^\mathrm{c}(i\omega) \simeq P_n(i\omega) := \sum_{j=1}^{N_\mathrm{poles}} \frac{a_{n,j}}{i\omega+b_{n,j}} + a_{n,0}\,. \tag{25}$$

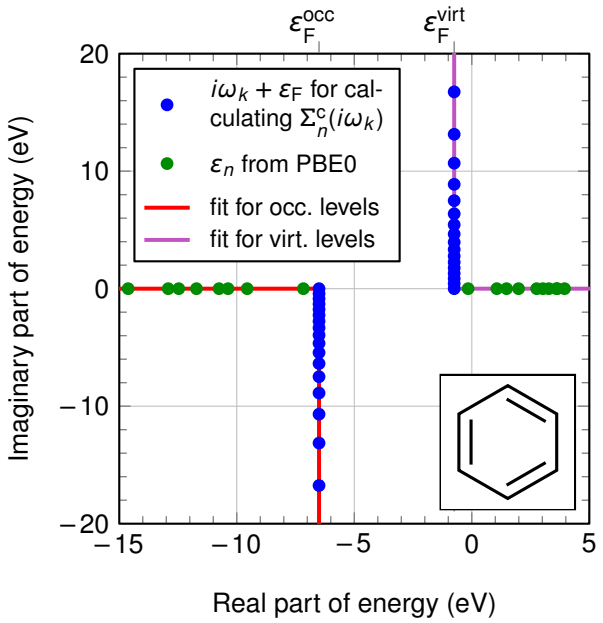

Figure 1: Clenshaw-Curtis grid points $i\omega_k$ (blue dots), fit of the self-energy [Eq. (24)] on imaginary frequencies (red and magenta lines) and evaluation of the fitting function at the GKS eigenvalues ε_n (green dots). We set the Fermi level ε_F in Eq. (24) as $\varepsilon_\mathrm{HOMO} + 0.3\,\mathrm{eV}$ for occupied orbitals and as $\varepsilon_\mathrm{LUMO} - 0.3\,\mathrm{eV}$ for virtual orbitals.

The complex coefficients $a_{n,j}$ and $b_{n,j}$ are determined by a nonlinear least-square fit, solved with a Levenberg-Marquardt algorithm. During the fitting procedure, we apply the constraint $P_n(0) = \Sigma_n^\mathrm{c}(i0)$ to fix the fit at $\omega = 0$ to the computed self-energy $\Sigma_n^\mathrm{c}(i0)$. To avoid branch cuts, the self-energy of an occupied orbital n is fitted for negative imaginary frequencies while the self-energy of a virtual orbital is fitted for positive imaginary frequencies, see Fig. 1.[107,108] As also sketched in Fig. 1, we set the Fermi level ε_F in Eq. (24) for occupied orbitals n as $\varepsilon_\mathrm{F} = \varepsilon_\mathrm{HOMO} + 0.3\,\mathrm{eV}$ and for virtual orbitals n as $\varepsilon_\mathrm{F} = \varepsilon_\mathrm{LUMO} - 0.3\,\mathrm{eV}$. The advantage of this procedure is that the fit has an anchor point $\Sigma_n^\mathrm{c}(i0)$ close to the eigenvalues ε_n of the SCF, see Fig. 1.

By replacing $i\omega$ with ω in P_n in Eq. (25), the self-energy can be evaluated on the real-frequency axis. Then, Eq. (3) to determine the quasiparticle energies turns into the working

expression

$$\varepsilon_n^{G_0W_0} = \varepsilon_n + Z_n \left[\Sigma_n^{\mathrm{x}} + \mathrm{Re}\, P_n(\varepsilon_n - \varepsilon_{\mathrm{F}}) - v_{nn}^{\mathrm{xc}}\right] , \tag{26}$$

with $Z_n = 1/[1 - \mathrm{Re}\, P_n'(\varepsilon_n - \varepsilon_{\mathrm{F}})]$ and the diagonal element v_{nn}^{xc} of the exchange-correlation matrix.

3 G_0W_0 benchmark calculations

In this section, we report G_0W_0 benchmark results to validate our G_0W_0 implementation. The section is organized as follows: In Sec. 3.1, we give the computational parameters which have been used for all calculations. Then, we investigate the convergence of the benzene-G_0W_0-HOMO energy and the G_0W_0-HOMO-LUMO gap with respect to the most important numerical parameters (Sec. 3.2). Execution times, parallel speedup and the system size scaling of our implementation are reported in Sec. 3.3. As application of our G_0W_0 implementation, we study the influence of different ligands on the gap of CdSe nanoclusters and we compare G_0W_0-HOMO energies of small molecules to experimental values and other G_0W_0 implementations (Sec. 3.4).

3.1 Computational details

For all calculations reported here, we employ the Gaussian and plane waves scheme (GPW)[50] for the underlying generalized Kohn-Sham (KS) equations as implemented in CP2K[51,52,111–113]. The GPW scheme makes use of a Gaussian basis to expand molecular orbitals and an auxiliary plane-wave basis for the expansion of the electronic density. This dual representation allows for evaluating the Hartree contribution to the KS matrix in linear scaling time at full accuracy.[111] In order to have an efficient expansion of the density in plane waves, core electrons are replaced by pseudopotentials. We use dual-space pseudopotentials of the Goedecker-Teter-Hutter (GTH) type[114,115] specifically parameterized for LDA[116], PBE[76],

PBE0[64] and B3LYP[65].

Regarding the Gaussian basis, we employ valence-only correlation-consistent basis sets[117,118], generated specifically for the use with GTH pseudopotentials[119]. The basis sets have been labeled as cc-DZVP, cc-TZVP, cc-QZVP and cc-5ZVP, denoting double, triple, quadruple and quintuple-zeta quality, respectively. For each primary basis set, the corresponding auxiliary RI basis has been generated[54] according to the procedure proposed by Weigend *et al.*[120]

The plane-wave cutoff for the DFT part of the calculations is $E_{\text{cut}} = 1200\,\text{Ry}$ to guarantee convergence of the SCF, at small cost compared to the GW calculations. For the calculations of two- and three-center ERIs for GW, we employed a high quality plane-wave cutoff of $E_{\text{cut}} = 300\,\text{Ry}$ for the expansion of the RI fitting densities. Gas phase systems have been computed using cluster boundary conditions for solving the Poisson equation[121].

As input geometries for the SCF and the subsequent G_0W_0 calculations, we take B3LYP-relaxed molecular geometries from the CCCBDB database[122]. As general computational G_0W_0 setup, we use 100 grid points for the frequency integration in Eq. (24) and a Fermi level which is 0.3 eV above $\varepsilon_{\text{HOMO}}$ for occupied MOs and 0.3 eV below $\varepsilon_{\text{LUMO}}$ for virtual MOs. The range for fitting the correlation self-energy [Eq. (25)] is chosen as $[0, \pm 10\,\text{eV}]i$ on the imaginary-frequency axis, where '$-$' refers to quasiparticles and '$+$' to quasiholes.

3.2 Convergence of numerical parameters: the benzene molecule

In this section, we present convergence tests of the HOMO level and the HOMO-LUMO gap of benzene for the PBE0 starting point with respect to the main computational parameters. Similar convergence has been obtained for other systems and different starting wavefunctions. We are also testing auxiliary density matrix methods (ADMM)[123,124] for the approximate, but faster computation of exact exchange at the SCF level. The reference value for benzene is $\varepsilon_{\text{HOMO}}^{G_0W_0@\text{PBE0}} = -9.29\,\text{eV}$, which has been obtained employing the cc-5ZVP basis and numerical parameters as described in the previous section. Our reference is in good agreement with the experimental vertical ionization potential of 9.24 eV[125] and G_0W_0@PBE0 HOMO energies

from other implementations (−9.20 eV from Ref. 1 and −9.32 eV from Ref. 46).

3.2.1 Primary basis set

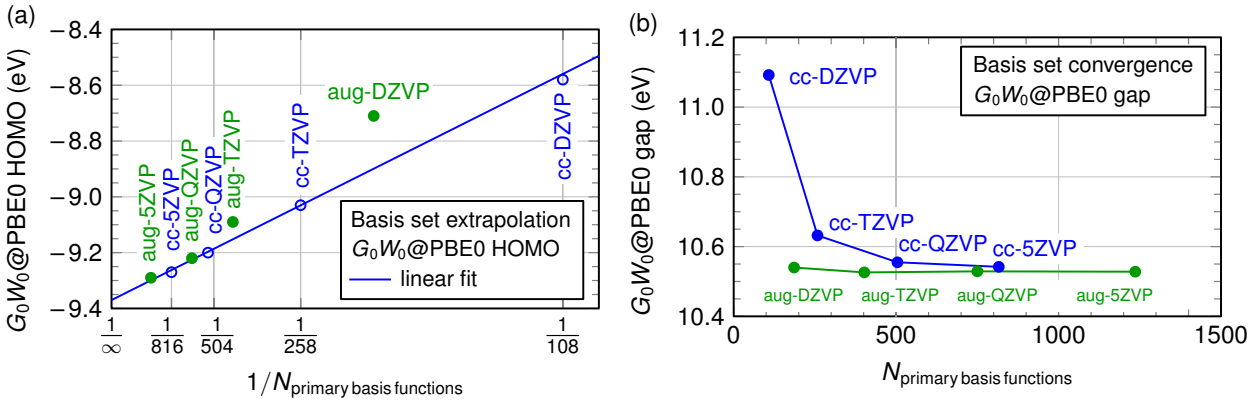

Figure 2: (a) Extrapolating the basis set size of the G_0W_0@PBE0 HOMO energy of benzene in the correlation-consistent (cc) basis. As comparison, we show the basis set convergence in the augmented (aug) basis. We observe that an accuracy of 0.1 eV compared to the complete-basis limit is only reached at the level of a cc-5ZVP basis set. (b) G_0W_0@PBE0 HOMO-LUMO gap of benzene for various cc and aug basis sets. We observe that the convergence of the G_0W_0-HOMO-LUMO gap in an augmented Gaussian basis is already reached using an aug-DZVP basis with an accuracy below 0.02 eV compared to the complete basis-set limit.

In Figure 2 (a), the convergence and the extrapolation of the G_0W_0@PBE0-HOMO energy with the size of the basis set is sketched. As previously reported in the literature[2,9,12,14], the convergence of single G_0W_0 quasiparticle levels in a Gaussian basis is very slow. An accuracy of 0.1 eV compared to the complete-basis limit is only reached at the level of a cc-5ZVP basis set, which means as many as 816 basis functions for the benzene molecule.

Figure 2 (b) displays the convergence of the G_0W_0@PBE0-HOMO-LUMO gap with the size of the basis set. As previously reported in the literature[6,8,14,20,21], the convergence of the G_0W_0-HOMO-LUMO gap in an augmented Gaussian basis is very fast and already reached using an aug-DZVP basis with an accuracy of less than 0.02 eV for benzene. In contrast, the HOMO-LUMO gap converges much slower employing a correlation-consistent basis without augmentation functions.

3.2.2 RI-basis set

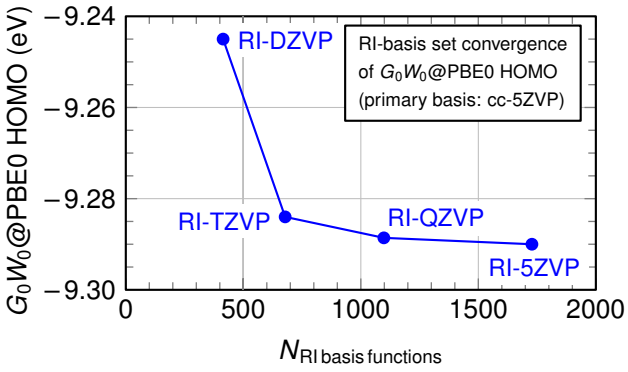

Figure 3: G_0W_0@PBE0 HOMO of benzene for the cc-5ZVP basis and various RI-basis sets. The RI-basis sets contain Gaussians of angular momenta up to $l_{\text{RI-DZVP}} = 3$, $l_{\text{RI-TZVP}} = 4$, $l_{\text{RI-QZVP}} = 5$ and $l_{\text{RI-5ZVP}} = 6$, respectively. We observe that an RI-QZVP basis already reaches convergence for a cc-5ZVP primary basis with a precision < 0.001 eV.

Figure 3 shows the convergence of the G_0W_0@PBE0-HOMO energy with the size of the RI-basis set for benzene. As primary basis, we use the cc-5ZVP basis. The RI basis sets have been generated specifically for GTH pseudopotentials[54] employing the procedure of Weigend and co-workers[120]. The maximum angular momentum of the RI basis is identical to the RI basis sets of Weigend *et al.*[120] and the size of the RI basis is similar to Ref. 120. As it can be seen in Fig. 3, an RI-QZVP basis already reaches convergence for a cc-5ZVP primary basis when computing the G_0W_0@PBE0-HOMO energy: The difference between the G_0W_0@PBE0-HOMO energy with the RI-QZVP and the RI-5ZVP basis is less than 0.001 eV. Since the overall execution time of our G_0W_0 scheme scales quadratically with the number of RI basis functions for large systems, the computational cost for a cc-5ZVP basis set may be reduced by a factor of two for large systems when using the RI-QZVP basis instead of the RI-5ZVP basis without significant loss of accuracy. We conclude that the computational cost can be reduce by employing a smaller RI basis but the angular momentum components have to be chosen carefully in order to properly fit the primary basis. Clever RI basis sets are minimum in size and tuned properly with angular momentum.

3.2.3 Auxiliary density matrix method (ADMM)

In ADMM[123,124], an approximate auxiliary density matrix is employed to compute the exact Hartree-Fock exchange at the SCF level. For the auxiliary density matrix, a smaller Gaussian basis is used compared to the Gaussian basis in the SCF. When employing the ADMM methodology, the cost and memory for computing the exact exchange in the SCF can be reduced significantly.

The auxiliary density matrix can be derived from several schemes named ADMM1[123], ADMM2[123], ADMMQ[124], ADMMP[124] and ADMMS[124]. In ADMM1, the MOs in the auxiliary basis remain orthogonal, while in ADMM2 this is not the case in order to allow a higher flexibility for the auxiliary fitting basis. As consequence, the ADMM2 auxiliary density matrix is purified to restore the idempotency of density matrices. In ADMMQ, the particle number in the auxiliary density matrix is constrained to the particle number of the full density matrix. In ADMMS and ADMMP, the particle number in the auxiliary basis is also constrained and scaling laws of exchange are respected in two ways which are different for ADMMS and ADMMP.

Here, the influence of ADMM on the G_0W_0 quasiparticle energies is tested when using the ADMM approximation in computing the reference PBE0 wavefunctions. The reason for testing ADMM is that for a high-quality basis as needed for G_0W_0, the computation of the exact exchange at the SCF level can by far dominate in the total execution time.[1]

Figure 4 displays the G_0W_0@PBE0-HOMO energy in case ADMM has been employed in the SCF while exact exchange with the full primary basis has been used for the exchange self-energy in Eq. (26). We observe that irregardless of the ADMM scheme, the G_0W_0@PBE0-HOMO energy of benzene differs by 0.03 eV between exact Fock exchange in the SCF and an

[1]The reason for the high computational cost for computing the exact exchange in the SCF is, that during the SCF procedure, the ERIs are needed in each cycle while at the G_0W_0 level, the computation of the ERIs for the exact-exchange Fock matrix elements has to be performed only once. For a high quality basis, the screening in the computations of the ERIs is not efficient and the available memory can thus not be enough for their complete storage, meaning that part of them have to be recomputed at each SCF cycle making the SCF computationally more demanding than the G_0W_0 quasiparticle energy evaluation.

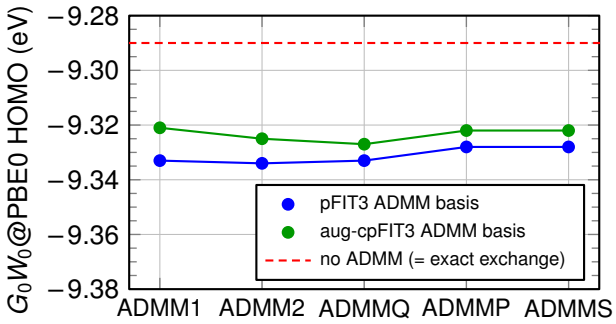

Figure 4: G_0W_0@PBE0 HOMO of benzene for an approximative treatment of the exact exchange in the SCF for five auxiliary density matrix methods (ADMM)[123,124]. The exchange self-energy in Eq. (26) is treated exactly without ADMM. Both auxiliary ADMM basis functions contain basis functions up to $l = 3$, where aug-cpFIT3 contains more basis functions than pFIT3. We observe that irregardless of the ADMM scheme, the G_0W_0@PBE0-HOMO energy of benzene differs by 0.03 eV between exact Fock exchange in the SCF and an ADMM-treated Fock exchange in the SCF.

ADMM-treated Fock exchange in the SCF. Since the systems considered in this work are not prohibitively large for exact exchange calculations, we treat the Fock exchange exactly[97,98] throughout this work.

3.2.4 Grid for frequency integration, fitting range and number of poles

The correlation self-energy $\Sigma^c(i\omega)$ on the imaginary-frequency axis, with a fixed value of ω, is obtained by numerical integration of Eq. (24). Consistently to the way the RPA correlation energy is computed[54], a Clenshaw-Curtis grid[105,106] $\{\omega_k\}$ is employed with a fixed scaling parameter[106] $a = 0.2$ Hartree. The same grid $\{\omega_k\}$ is employed for ω' and ω in Eq. (24), meaning that the self-energy $\Sigma^c(i\omega)$ is evaluated at the same frequencies ω as those employed for the numerical integration over ω'. Subsequently, $\Sigma^c(i\omega_k)$ is fitted with the two-pole model of Eq. (25). According to the target accuracy, an ω-interval is defined and only the ω_k points that are contained in this range are employed for the fitting procedure.

Figure 5 displays the convergence of the G_0W_0@PBE0 HOMO energy of benzene with respect to the number of grid points for different fitting intervals of $\Sigma^c(i\omega)$. The drawback of using a large fitting interval is that for an ω_j with large absolute value, $\Sigma^c(i\omega_j)$ is calculated

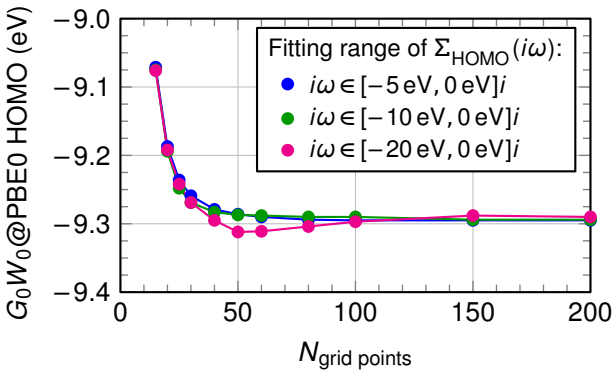

Figure 5: G_0W_0@PBE0 HOMO of benzene for different numbers of Clenshaw-Curtis integration grid points of Eq. (24) and for three intervals on the imaginary axis for the fitting procedure in Eq. (25). For a fitting range of $[-10\,\text{eV}, 0\,\text{eV}]i$ and 50 grid points, we obtain a result being converged with a precision $< 0.01\,\text{eV}$.

with lower accuracy compared to $\Sigma^c(i\omega_j)$ with smaller absolute value $|\omega_j|$. The reason is that the integrand in Eq. (24) is large for $\omega_j = \omega'_j$ but the resolution of the $\{\omega'_k\}$ grid around ω_j with large $|\omega_j|$ is coarse, see e. g. Fig. 1. The consequence of this issue is seen in Fig. 5 for the large fitting interval $[-20\,\text{eV}, 0\,\text{eV}]i$: The HOMO energy converges more slowly and non-monotonously compared to the smaller fitting intervals. On the other hand, a too small fitting interval may miss the structure of Σ^c on the imaginary-frequency axis. Consequently, we take a medium fitting interval of $[-10\,\text{eV}, 0\,\text{eV}]i$ for all calculations presented in this work.

Moreover, we observe in Fig. 5 that with 50 grid points and a fitting interval of $[-10\,\text{eV}, 0\,\text{eV}]i$, the HOMO energy is converged with an accuracy of $< 0.01\,\text{eV}$. To ensure high-quality results, we use 100 grid points for all following calculations.

The fit of the correlation self-energy on the imaginary-frequency axis is performed by using a multi-pole model employing a given number of poles N_{poles}, see Eq. (25). Figure 6 displays the G_0W_0@PBE0 HOMO energy of benzene for various numbers of poles used. In agreement with previous works[1,13], we find that two poles for the fitting procedure are already sufficient: the result changes by less than 0.005 eV for three or more poles compared to two poles. As consequence, we take two poles for all following calculations.

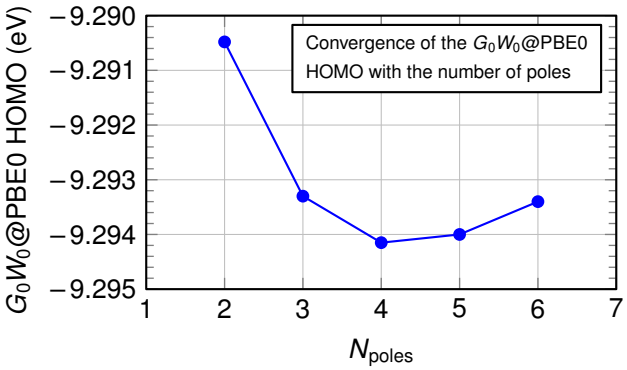

Figure 6: G_0W_0@PBE0 HOMO of benzene as function of the number of fitting poles N_{poles} in Eq. (25). We observe that two poles are already sufficient for the fitting procedure: The result changes by less than 0.005 eV for three or more poles compared to two poles.

3.2.5 Fermi level

The Fermi level ε_{F} is needed in order to compute the Green's function for imaginary frequencies, see Eq. (24). As sketched in Fig. 1, we set the Fermi level ε_{F} in Eq. (24) for occupied orbitals n as $\varepsilon_{\text{F}} = \varepsilon_{\text{HOMO}} + 0.3\,\text{eV}$ and for virtual orbitals n as $\varepsilon_{\text{F}} = \varepsilon_{\text{LUMO}} - 0.3\,\text{eV}$. In principle, the Fermi level may be chosen arbitrarily between the HOMO and the LUMO energy of the underlying GKS calculation. Indeed, we observe in Fig. 7, that as long as the Fermi level is located more than 0.1 eV above the HOMO energy of the SCF, we get identical results for the benzene G_0W_0@PBE0 HOMO energy. Due to the numerical issues seen for $\delta < 0.1\,\text{eV}$ in Fig. 7, G_0W_0 calculations for a system with a GKS gap smaller than 0.2 eV need a careful treatment within our methodology.

3.2.6 Geometry optimization

Prior to a G_0W_0 calculation, it is a common practice to relax the ground state geometry employing the same KS method as used to generate the input orbitals for the G_0W_0 calculation. For hybrid functionals, the computation of the exact HF exchange can be significantly more expensive such that the geometry optimization would be more costly than the subsequent G_0W_0 calculation. Here, we examine the influence of the input geometry on the G_0W_0@PBE0 HOMO energy, see Fig. 8. The geometries have been obtained by a structure optimization with

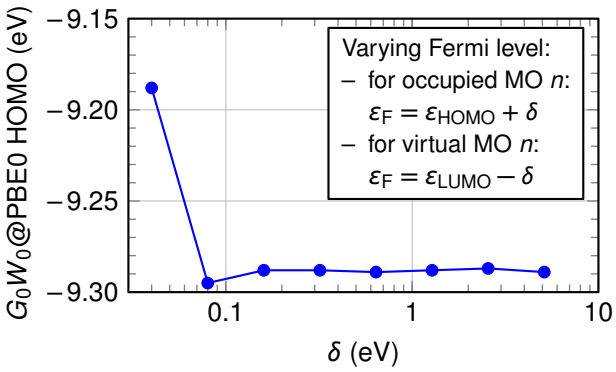

Figure 7: G_0W_0@PBE0 HOMO of benzene as function of a varying Fermi level ε_F in the Green's function in Eq. (24). We observe in Fig. 7 that as long as the Fermi level is located more than 0.1 eV above the HOMO or 0.1 eV below the LUMO energy, we get identical results for the benzene G_0W_0@PBE0 HOMO energy.

the PBE and the PBE0 functional, respectively and various basis sets, while the G_0W_0@PBE0 HOMO is obtained using the cc-5ZVP basis. As shown in Fig. 8 (a), the structure relaxation with a cc-TZVP is sufficiently close to the complete-basis limit. Moreover, we find that the G_0W_0@PBE0 HOMO level differs by 0.04 eV between structures relaxed at the PBE and PBE0 level (or other hybrids). We conclude that using a non-hybrid functional for the geometry optimization may introduce a non-negligible systematic error in G_0W_0@PBE0 quasiparticle energies. In order to reduce the cost necessary to generate the initial geometry, a small primary basis at the triple-zeta level can be used to obtain converged quasiparticle energies.

3.3 Execution time, system size scaling and parallel speedup

For an exemplary benchmark of the computational cost, we show the execution time for computing 20 G_0W_0 quasiparticle energies (HOMO–9, HOMO–8, ..., LUMO+9) for various water clusters in Fig. 9 (a) (without the time spent for the GKS calculation) employing $N_\omega = 60$ grid points for the frequency integration in a cc-TZVP basis.

According to Eq. (22), the computation of $\Pi_{PQ}(i\omega)$ for all grid points ω_k requires $N_{\text{aux}}^2 N_{\text{occ}} N_{\text{virt}} N_\omega$ operations, where N_{aux} is the number of auxiliary RI-basis functions, N_{occ}

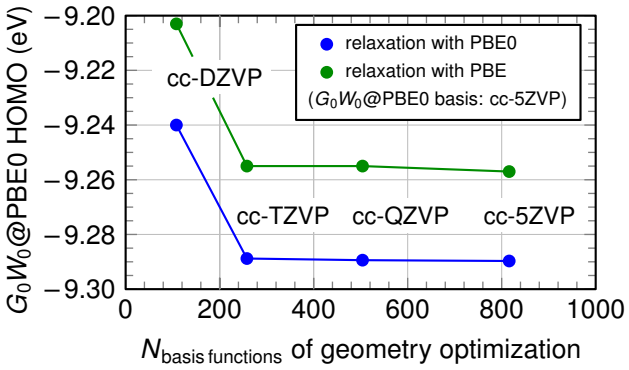

Figure 8: G_0W_0@PBE0 HOMO of benzene for various geometries. The geometries have been obtained by a geometry optimization with the PBE0 (blue dots) and the PBE functional (green dots). The basis set for the G_0W_0 calculation is of cc-5ZVP quality. We observe that a structure relaxation with a cc-TZVP basis is sufficiently close to the complete-basis limit. Moreover, we find that the G_0W_0@PBE0 HOMO level differs by 0.04 eV for the structures obtained with the PBE and the PBE0 functional for the structure relaxation, respectively.

(N_{virt}) the number of occupied (virtual) molecular orbitals and N_ω the number of Clenshaw-Curtis grid points. Assuming N_ω to be independent on the system size N, this step scales as $\mathcal{O}(N^4)$. The measured exponent is 3.93, see Fig. 9 (a) and therefore matching the expected value. Note that once $\Pi_{PQ}(i\omega)$ is made available for all ω_k, the computation of $\Sigma_n^{\text{c}}(i\omega)$ in Eq. (24) requires only $\mathcal{O}(N^3)$ operations, more specifically $N_{\text{aux}}^2 N_{G_0W_0}(N_{\text{occ}}+N_{\text{virt}})N_\omega$, where $N_{G_0W_0}$ is the number of computed G_0W_0 quasiparticle energies. We observe an exponent of 3.34 in Fig. 9 (a) which is slightly exceeding the expected exponent of 3. According to this analysis, we expect a numerical effort for the overall computation of the G_0W_0 quasiparticle energies which asymptotically scales as $\mathcal{O}(N^4)$. This is what we observe as total execution time for our G_0W_0 algorithm, see Fig. 9 (a): The computational effort for the integral evaluation part has an asymptotic scaling that grows quadratically with system size: For each auxiliary RI density, only matrix elements between overlapping Gaussian functions need to be calculated. For this reason, the effort for the integral evaluation strongly depends on the structure of the system, since this affects the overlap between the atom-centered Gaussian basis functions and thus is directly related to the effectiveness of the screening on the matrix elements. For small and compact systems, the integral evaluation is in general dominating the

overall time of a G_0W_0 calculation[54]. On the other hand, in the evaluation of $\Pi_{PQ}(i\omega)$, that scales $\mathcal{O}(N^4)$ with system size, no screening is considered and thus this part is independent on the actual structure of the system. This part is by far the most time consuming in a large G_0W_0 calculation[55].

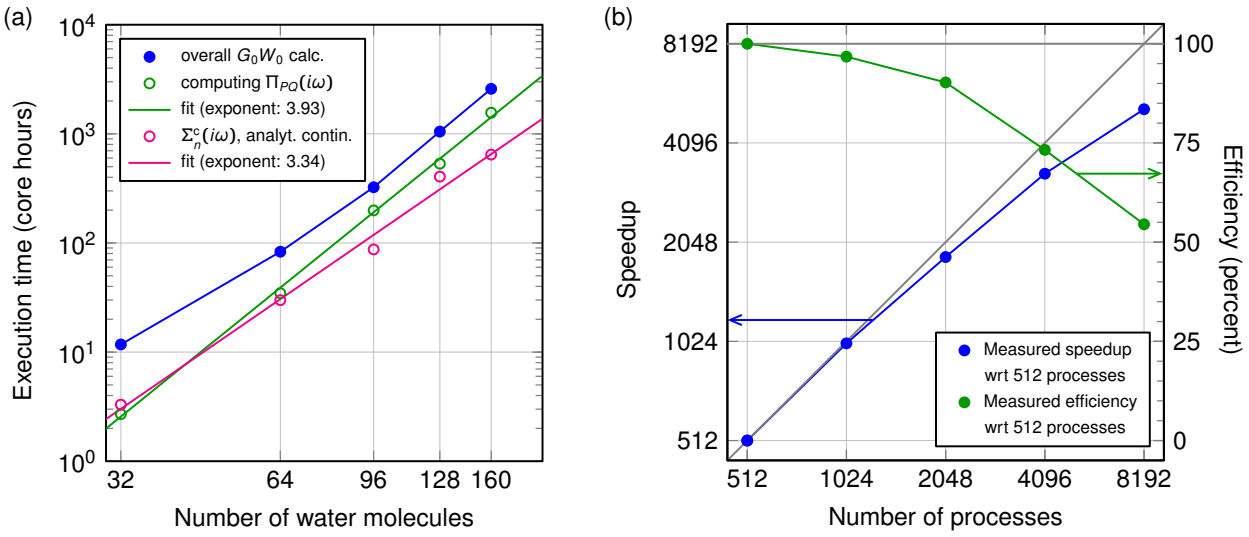

Figure 9: (a) Execution time for the calculation of 20 G_0W_0 quasiparticle levels of water clusters containing up to 480 atoms in a cc-TZVP basis with 60 grid points for the numerical integration of Eq. (24) on a Cray XC30 machine. The blue dots belong to the time spent for the whole G_0W_0 calculation (without the time spent for the SCF), the green circles belong to the time for computing the matrix $\Pi_{PQ}(i\omega)$ [Eq. (22)] and the magenta circles belong to the computation time of the self-energy [Eq. (24)] and the analytic continuation. The magenta and green lines represent a linear two-parameter fit of the form $y = ax^b$ with an exponent b as reported in the legend. (b) Measured speedup (blue dots, left ordinate) and efficiency (green dots, right ordinate) with respect to 512 processes for the calculation of 20 G_0W_0 quasiparticle energies of a 64 water-molecule cluster. We used a cc-TZVP basis and 60 grid points for the numerical integration of Eq. (24). The gray lines represent the ideal speedup and the ideal efficiency, respectively.

We assess the parallel speedup of our implementation with a cluster containing 64 water molecules (256 occupied orbitals, 3392 virtual orbitals and 8704 auxiliary basis functions), see Fig. 9 (b). Our algorithm shows a good parallel scalability with an efficiency around 70 % for 4096 processes compared to 512 processes. The total execution time of the G_0W_0 calculation with 512 processes is 606 seconds, while the G_0W_0 calculation is completed in 70 seconds employing 8192 processes.

3.4 Comparison to experiments and other G_0W_0 implementations

In this section, we compare G_0W_0-HOMO energies of small molecules to experimental values and other GW implementations. Additionally, we apply G_0W_0 to study the influence of different ligands on the gap of CdSe nanoclusters.

3.4.1 HOMO levels of molecules

Table 1: G_0W_0 HOMO energy $\varepsilon_{\mathrm{HOMO}}^{G_0W_0}$ of small molecules containing atoms from the first period. We present results for the PBE[76], PBE0[64] and the tuned CAM-B3LYP[60,65,126] (tCB) starting point. The experimental vertical ionization potentials (VIPs) are taken from Ref. 66 besides the one of methane[127]. The mean absolute deviation (MAD) measures the deviation with respect to the experimental VIPs and the G_0W_0 HOMO energies reported by Ren *et al.*[1], Bruneval and Marques[2], Govoni and Galli[46], Turbomole without RI and full-frequency (ff) BerkeleyGW from the GW100 benchmark by van Setten *et al.*[49] The unit of all numbers is eV.

Molecule	G_0W_0@PBE		G_0W_0@PBE0		G_0W_0@tCB		Exp. VIP
Basis set	cc-QZVP	cc-5ZVP	cc-QZVP	cc-5ZVP	cc-TZVP	cc-QZVP	
C_6H_6	−9.00	−9.07	−9.21	−9.29	−9.33	−9.51	−9.24
CH_4	−14.00	−14.05	−14.28	−14.33	−14.47	−14.59	−14.40
C_2H_2	−11.01	−11.11	−11.25	−11.33	−11.35	−11.52	−11.49
C_2H_5OH	−10.26	−10.35	−10.63	−10.73	−10.77	−10.99	−10.64
CO_2	−13.20	−13.33	−13.58	−13.72	−13.64	−13.85	−13.78
N_2	−14.87	−15.03	−15.37	−15.52	−15.44	−15.66	−15.58
NH_3	−10.29	−10.42	−10.64	−10.75	−10.80	−11.00	−10.82
H_2O	−11.97	−12.13	−12.33	−12.46	−12.46	−12.72	−12.62
O_2	−11.65	−11.83	−12.24	−12.40	−12.43	−12.70	−12.30
MAD to exp. VIPs	0.51	0.39	0.15	0.09	0.12	0.21	
MAD to FHI-aims[1] (tier+a5Z-d basis)	0.02	0.10	0.05	0.07	–	–	
MAD to molgw[2] (QZVP basis)	0.06	0.04	0.04	0.04	0.18	0.08	
MAD to WEST[46] (PW basis)	0.09	0.11	0.11	0.03	–	–	
MAD to Turbomole[49] (QZVP basis)	0.03	0.11	–	–	–	–	
MAD to ff BerkeleyGW[49] (PW basis)	0.14	0.26	–	–	–	–	

As generalized Kohn-Sham (GKS) starting points for the G_0W_0 calculation of molecules, we consider PBE[76], PBE0[64], which contains 25 % exact exchange, and tuned CAM-B3LYP[65,126], a range-separeted hybrid functional as implemented in the exchange-correlation library LIBXC, version 2.2.2[60] with 100 % exact long-range exchange. It has been reported in the literature that G_0W_0 HOMO energies are in excellent agreement with experimental vertical

ionization potentials (VIPs) and CCSD(T) values if the GKS calculation was performed with the tuned CAM-B3LYP functional[2,21,128] or the PBE0 hybrid functional[1,2,14,22,46,61–64,76] while local functionals as PBE or pure Hartree-Fock perform worse[1,2].

For PBE, PBE0 and tuned CAM-B3LYP, the G_0W_0 HOMO energies of small molecules are listed in Table 1. The results indicate that for the G_0W_0@PBE0 HOMO energies, the large basis cc-5ZVP provides the best agreement with experimental values: The observed mean absolute error is below 0.1 eV compared to the experimental vertical ionization potential (VIP). In contrast, the best agreement with experimental VIPs for G_0W_0@tuned CAM-B3LYP HOMO energies are obtained within the cc-TZVP basis. The larger cc-QZVP basis deteriorates the mean absolute error compared to experimental VIPs. We mention that the accuracy of inner orbitals (higher IPs) in G_0W_0 is of similar accuracy as reported here for the HOMO[61].

Overall, our results agree well with the results reported by Ren *et al.*[1], Bruneval and Marques[2], Govoni and Galli[46] and from *GW*100[49,129], see Table 1. Possible differences are due to our use of pseudopotentials and the differing basis.

3.4.2 G_0W_0 HOMO-LUMO gaps of $Cd_{33}Se_{33}$ nanoclusters in the presence of ligands

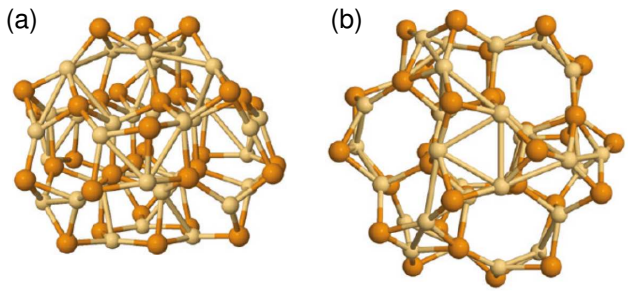

Figure 10: Molecular structure of the bare $Cd_{33}Se_{33}$ nanocluster: (a) side view and (b) top view.[130] The Cd is light yellow and the Se is bronze in the ball-and-stick models.

In this section, we apply G_0W_0@LDA and G_0W_0@PBE to compute the HOMO-LUMO gap of the $Cd_{33}Se_{33}$ nanocluster with different surrounding ligands, see Fig. 10 for the molecular

geometry of the bare $Cd_{33}Se_{33}$ cluster. At best of our knowledge, no *GW* calculations have been reported in the literature on the $Cd_{33}Se_{33}$ nanocluster.

We are motivated by the fact that CdSe has been one of the most studied II-VI quantum dots due to the ease of synthesis and, according to the dimension of the QDs, its optical gap can cover the visible spectrum.[131,132] We chose the $Cd_{33}Se_{33}$ quantum dot since it is one of the "magic-size" clusters that have been characterized by high stability and large optical gaps. For quantum dots, surface ligands are fundamental for enhancing the solubility and for stabilizing the core structure. Here, the ligands can strongly affect the electronic properties of the quantum dots, in particular the optical gap.[133–138] We investigate the influence of these surface ligands on the HOMO-LUMO gap of $Cd_{33}Se_{33}$ quantum dots on the level of G_0W_0@LDA and G_0W_0@PBE. As model ligands, we employ formic and acetic acid, ammonia and methyl amine.[130]

As molecular geometries of the bare $Cd_{33}Se_{33}$ cluster and $Cd_{33}Se_{33}$ with ligands, we employ the structures from Ref. 130: The bare cluster has been obtained by carving out an almost spherical portion of the wurtzite lattice with bulk CdSe bond lengths and subsequent relaxation on the level of LDA[116]. Similar constructions of CdSe clusters from the bulk semiconductor have been used in previous theoretical studies.[133,134,139,140] The cages in presence of the ligands have been fully relaxed on the LDA level. We employ GTH[114,115] pseudopotentials. In the SCF, we optimize twelve electrons for Cd and six electrons for Se.

We employ G_0W_0@LDA and G_0W_0@PBE to compute the HOMO-LUMO gap of the $Cd_{33}Se_{33}$ nanocluster. Here, we follow the authors of Refs. 16 and 46 who employed G_0W_0@LDA and G_0W_0@PBE for computing the HOMO-LUMO gap of silicon nanoclusters. We employ an aug-DZVP basis set which is listed in the supporting information. In this basis set, we expect G_0W_0 HOMO-LUMO gaps which are close to the complete-basis-set limit[6,8,14,20,21].

We have computed the HOMO-LUMO gap of the $Cd_{33}Se_{33}$ nanocluster in the bare form and with ligands on different levels of theory, see results in Table 2. For the bare cluster, we

Table 2: LDA, G_0W_0@LDA, PBE and G_0W_0@PBE HOMO-LUMO gaps in eV of $Cd_{33}Se_{33}$ nanoclusters with surrounding ligands in an aug-DZVP basis set. Exemplarly, for the $Cd_{33}Se_{33}$ nanocluster, 594 non-core electrons (12 electrons per Cd atom, 6 electrons per Se atom), 2574 primary basis functions and 8316 RI basis functions have been employed. This calculation took 15 minutes on 1536 Cray XC40 cores.

System	LDA	G_0W_0@LDA	PBE	G_0W_0@PBE	Exp. optical gap
bare $Cd_{33}Se_{33}$	1.51	3.64	1.60	3.62	3.0 [141]
$Cd_{33}Se_{33}$ + 9 NH_3	1.57	3.59	1.70	3.56	
$Cd_{33}Se_{33}$ + 12 NH_3	1.61	3.60	1.73	3.60	
$Cd_{33}Se_{33}$ + 21 NH_3	1.75	3.69	1.87	3.69	
$Cd_{33}Se_{33}$ + 9 H_3CNH_2	1.56	3.56	1.68	3.56	
$Cd_{33}Se_{33}$ + 9 HCOOH	2.03	4.10	2.19	4.14	
$Cd_{33}Se_{33}$ + 9 HCOOH + 12 NH_3	2.03	4.06	2.20	4.10	
$Cd_{33}Se_{33}$ + 9 H_3CCOOH	2.00	4.05	2.16	4.09	

find an LDA and a PBE HOMO-LUMO gap of 1.51 eV and 1.60 eV, respectively. Both values strongly underestimate experiments with a measured optical gap of 3.0 eV of $Cd_{33}Se_{33}$ [141] probably due to the spurious self-interaction of the HOMO. In contrast, after one-shot G_0W_0@LDA and G_0W_0@PBE, the HOMO-LUMO gap opens up to 3.64 eV and 3.62 eV, respectively. Here, the G_0W_0 HOMO-LUMO gaps are compatible with the experimental optical gap in the sense that the experimental optical gap ist smaller than the G_0W_0 HOMO-LUMO gap due to the exciton binding energy. For a computation of the optical gap, the Bethe-Salpeter equation on top of G_0W_0 would be necessary.

For the $Cd_{33}Se_{33}$ cluster with ligands, electron-donating ligands as amines hardly affect the HOMO-LUMO gap of the $Cd_{33}Se_{33}$ nanocluster. This effect is seen on both levels of theory, LDA/PBE and G_0W_0. In contrast, the HOMO-LUMO gap of $Cd_{33}Se_{33}$ is strongly affected by electron-attracting ligands as formic acid. Again, this effect is seen on both levels of theory, LDA/PBE and G_0W_0. The influence of the ligands on the HOMO-LUMO gap of $Cd_{33}Se_{33}$ was already found in Ref. 130 by LDA and PBE calculations and we have validated this finding by G_0W_0.

4 Application of eigenvalue-selfconsistent *GW* to linear acenes

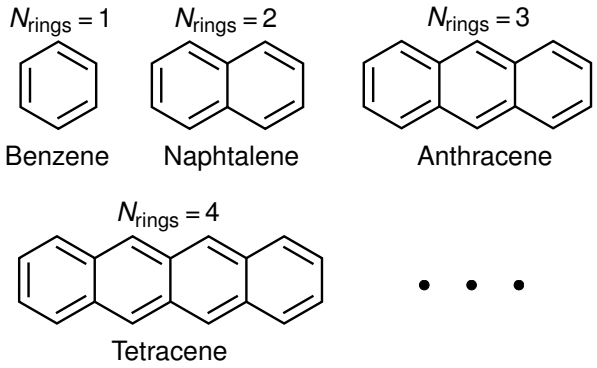

Figure 11: Molecular structure of the first acenes.

In this section, we apply eigenvalue-selfconsistent *GW* (ev*GW*) to compute the HOMO-LUMO gap of linear acenes, see Fig. 11 for the molecular geometry. This application is motivated by a recent DFT-based study by Korytár *et al.*[67] indicating that the HOMO-LUMO gaps of acenes may not decay monotonously with increasing number of benzene rings, but can oscillate. The key ingredient to obtain a reasonable ev*GW* HOMO-LUMO gap is to employ a proper electronic ground state. Concerning the ground state of acenes, contradictory findings have been reported, see Sec. 4.1. The main point of debate is whether the groundstate of acenes is a radical or not. For our ev*GW* HOMO-LUMO-gap calculations, we employ closed-shell and open-shell broken-symmetry DFT groundstates as described in the computational details in Sec. 4.2. Then, we compare ev*GW* HOMO-LUMO gaps of anthracene, tetracene and pentacene to experimental values (Sec. 4.3). In Sec. 4.4, we turn over to predict the HOMO-LUMO gap of long acenes employing ev*GW* based on closed-shell and open-shell broken-symmetry DFT groundstates. We find distinct differences between the closed- and the open-shell ev*GW* HOMO-LUMO gaps for long acenes. In future experiments, a comparison of measured HOMO-LUMO gaps and our calculated ev*GW* values may be helpful to identify whether the groundstate of the acene exhibits a closed-shell or polyradical

configuration.

4.1 Electronic groundstate of acenes

In DFT studies employing hybrid functionals, singlet broken-symmetry, spin-polarized ground states have been reported for acenes with $N_{\text{rings}} \geq 6$.[79] This finding can be rationalized by Clar's theory. For details, we refer to Ref. 142. Since a polyradical singlet groundstate is not described by a single Slater determinant, it is difficult to interpret whether DFT or Hartree-Fock based studies predict the correct spin configuration of the groundstate.

Two findings from density matrix renormalization group (DMRG) calculations, which incorporate multiple Slater determinants, have been reported: In the recent study by Korytár *et al.*[67], the DMRG with on-site and nearest-neighbor interactions indicates that the groundstate of acenes does not exhibit a (simple) broken-symmetry phase. Hachmann *et al.*[78] concluded in their DMRG study based on the full Coulomb interaction that longer acenes exhibit singlet polyradical character in their ground state. The latter finding was supported by multiconfiguration SCF calculations by Plasser *et al.*[77] Experimental evidence for the groundstate of longer acenes is missing since the synthesis of gas-phase acenes with more than six rings (hexacene) remains a challenge[143,144].

4.2 Computational details

We perform closed-shell and open-shell DFT calculations on the acenes as basis for geometry optimizations and the evGW calculations. For open-shell calculations, we initialize the wavefunctions with a singlet broken-symmetry guess and keep zero total spin during the SCF cycle. We obtain the oligoacene structures by a geometry optimization employing the PBE0[64] functional in a cc-TZVP basis.[2]

Eigenvalue-selfconsistent GW (evGW) calculations are performed as suggest by X. Blase *et*

[2]Geometry optimizations are performed with a closed-shell restriction for closed-shell evGW HOMO-LUMO gap calculations and with a singlet broken symmetry for open-shell evGW HOMO-LUMO gap calculations.

al.[6] In this methodology, the eigenvalues $\varepsilon_n^{G_0W_0}$ from Eq. (26) are employed to recompute the correlation self-energy and finally every eigenvalue. This procedure is repeated up to convergence and has been shown to give HOMO-LUMO gaps which are in good agreement with experimental values, especially for organic semiconductors with extended π-systems.[7] As starting points for the evGW calculations, we employ wavefunctions and eigenvalues from DFT calculations with the PBE0 and the tuned CAM-B3LYP functional. It has been pointed out by Bruneval and Marques[2] that both functionals are two of the most reliable starting points for GW calculations for molecules.

For the evGW HOMO-LUMO gap calculations, augmented basis sets are used. In augmented basis sets as the aug-DZVP and aug-TZVP, evGW HOMO-LUMO gaps are close to the complete-basis-set limit, see Fig. 2 (b) for benzene, the supporting information for acenes and the literature[6,8,14,20,21]. All other parameters are chosen as specified in Sec. 3.1 to ensure excellent convergence of the evGW results.

4.3 G_0W_0 and evGW HOMO-LUMO gaps of acenes compared to experiments

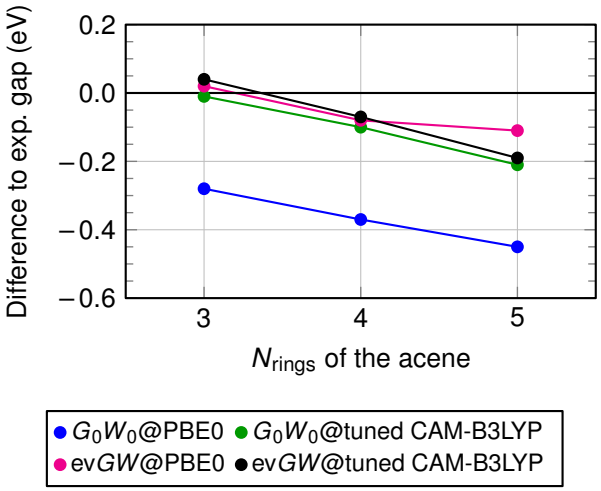

Figure 12: Deviation of the open-shell (broken-symmetry) G_0W_0 and eigenvalue-self-consistent GW[6] (evGW) HOMO-LUMO gap of acenes (aug-TZVP basis) from experimental HOMO-LUMO gaps. The raw data is listed in the supporting information.

In Fig. 12, we compare open-shell G_0W_0 and evGW HOMO-LUMO gaps of anthracene, tetracene and pentacene to experimental data[66]. It is important to note that the experimental assignment of the vertical IP in acenes is controversial and displays large error bars, see Ref. 145 and references therein. As an example, for the molecular crystal of tetracene, the error of the HOMO-LUMO gap is estimated to be 0.5 eV. We find that the G_0W_0@tuned CAM-B3LYP HOMO-LUMO gaps are close to experiment with a maximum deviation of 0.21 eV, while the G_0W_0@PBE0 HOMO-LUMO gaps exhibit an average error of 0.4 eV compared to experiments. After applying the self-consistency scheme on the eigenvalues as suggested by Blase *et al.*[6,7,20,146] (evGW), we find that HOMO-LUMO gaps of both starting points are in average agreement of 0.03 eV to each other which has already been reported by previous authors[6,145,147]. The mean absolute deviation of the evGW HOMO-LUMO gaps to the experimental HOMO-LUMO gaps remains below 0.1 eV for anthracene, tetracene and pentacene.

The difference of our values to previously reported evGW calculations on acenes in Refs. 6 and 128 can be attributed to the use of LDA wavefunctions[6] and PBE wavefunctions[128] as DFT input of evGW.

4.4 evGW HOMO-LUMO gaps of long acenes

We present HOMO-LUMO gaps of linear acenes computed with evGW for the PBE0 and the tuned CAM-B3LYP starting point, see Fig. 13. First, we observe, that for all acenes, the evGW HOMO-LUMO gaps based on PBE0 and tuned CAM-B3LYP starting points deviate by less than 0.10 eV (besides 10-acene and 11-acene in the closed-shell case). Second, we observe that the gaps of anthracene and tetracene ($N_{\text{rings}} = 3, 4$) are identical for closed-shell and open-shell calculations. The deviation between the closed-shell and open-shell evGW HOMO-LUMO gap of pentacene is below 0.1 eV. This finding can be rationalized by Clar's theory[142]: For small acenes, Clar's theory predicts a closed shell configuration, while for longer acenes, an open-shell configuration is expected to be favoured. In agreement with this

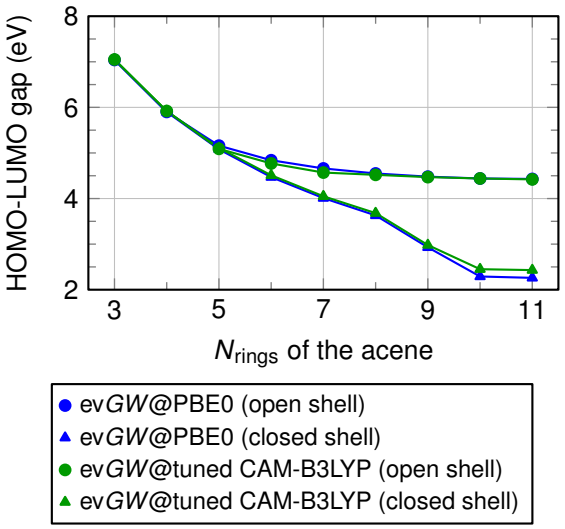

Figure 13: evGW HOMO-LUMO gap of acenes within an aug-DZVP basis for the PBE0 (blue) and the tuned CAM-B3LYP starting point (green) with broken-symmetry open-shell (circles) and closed-shell configuration (triangulars). We find that the evGW gaps are only weakly dependent on the starting DFT functional, but strongly dependent on restricting the DFT calculation to closed shell or not: The deviation of the evGW HOMO-LUMO gaps between open-shell and closed-shell can be as large as 2.0 eV (for 10-acene and 11-acene). The distinct jump of the evGW closed-shell gaps between 8-acene and 10-acene is in agreement with the DFT-based study by Korytár *et al.*[67] The reason is that close to the 9-acene, the symmetry of the HOMO and LUMO interchanges due to a level crossing in the bandstructure of polyacene[68] as elaborated in Ref. 67 The raw data is listed in the supporting information.

expectation, our (singlet) open-shell calculations on anthracene to pentacene converge to a closed-shell-like groundstate. As consequence, the evGW HOMO-LUMO gaps for anthracene to pentacene are (nearly) identical for the closed-shell and the open-shell calculation.

For longer acenes, the difference between the closed-shell and the open-shell evGW gaps is strongly increasing with a maximum of 2.0 eV for 10- and 11-acene: While the open-shell evGW gaps are quickly saturating between 4.4 and 4.6 eV for 7-acene to 11-acene, the closed-shell evGW gaps are rapidly decreasing from 4.0 eV (7-acene) to 2.3 eV or 2.4 eV (11-acene, evGW@PBE0 and evGW@tuned CAM-B3LYP). We conclude that a measurement of the HOMO-LUMO gap of longer acenes ($N_{\text{rings}} \geq 6$) may be able to identify whether the groundstate of the acene exhibits a closed-shell or polyradical configuration.

5 Conclusions

We have presented a G_0W_0 and eigenvalue-selfconsistent GW (evGW) implementation within the Gaussian and plane waves scheme. Technically, we calculate the correlation self-energy for imaginary frequencies employing a resolution-of-the-identity approach based on the Coulomb metric. The correlation self-energy for real frequencies is evaluated by analytic continuation. Our implementation is highly efficient and displays good parallel scalability enabling large-scale G_0W_0 and evGW calculations for systems containing hundreds of atoms.

We benchmarked our implementation for molecules and clusters. For molecules, we found an average error of 0.1 eV between the G_0W_0@PBE0-HOMO energy in a 5ZVP basis and the vertical ionization potential which is in agreement with previously published G_0W_0 data.

We applied evGW to compute the HOMO-LUMO gaps of closed-shell and open-shell broken-symmetry linear acenes as function of the oligoacene length up to 11-acene. We find that the closed-shell and broken-symmetry open-shell evGW HOMO-LUMO gaps of acenes differ by up to 2.0 eV (for 11-acene). In future experiments, a comparison of measured HOMO-LUMO gaps and our calculated evGW values may be helpful to determine whether

the electronic groundstate exhibits a closed-shell or polyradical configuration.

Acknowledgement

We express our gratitude to Xavier Blase, Ferdinand Evers, Xinguo Ren, Leopold Talirz, and Joost VandeVondele for helpful discussions. Calculations were enabled by the Swiss National Supercomputing Center (CSCS) under project ID uzh1, s425 and mr2.

Supporting Information Available

The basis sets for computing the oligoacene and CdSe nanocluster HOMO-LUMO gaps and an exemplary input file of CP2K are available as supporting information. This material is available free of charge via the Internet at `http://pubs.acs.org/`.

References

(1) Ren, X.; Rinke, P.; Blum, V.; Wieferink, J.; Tkatchenko, A.; Sanfilippo, A.; Reuter, K.; Scheffler, M. New J. Phys. **2012**, 14, 053020.

(2) Bruneval, F.; Marques, M. A. L. J. Chem. Theory Comput. **2013**, 9, 324–329.

(3) van Setten, M. J.; Weigend, F.; Evers, F. J. Chem. Theory Comput. **2013**, 9, 232–246.

(4) Kühn, M.; Weigend, F. J. Chem. Theory Comput. **2015**, 11, 969–979.

(5) Ren, X.; Marom, N.; Caruso, F.; Scheffler, M.; Rinke, P. Phys. Rev. B **2015**, 92, 081104.

(6) Blase, X.; Attaccalite, C.; Olevano, V. Phys. Rev. B **2011**, 83, 115103.

(7) Faber, C.; Boulanger, P.; Attaccalite, C.; Duchemin, I.; Blase, X. Phil. Trans. R. Soc. A **2014**, 372, 20130271.

(8) Faber, C.; Boulanger, P.; Attaccalite, C.; Cannuccia, E.; Duchemin, I.; Deutsch, T.; Blase, X. Phys. Rev. B **2015**, 91, 155109.

(9) Bruneval, F. J. Chem. Phys. **2012**, 136, 194107.

(10) Foerster, D.; Koval, P.; Sánchez-Portal, D. J. Chem. Phys. **2011**, 135, 074105.

(11) Koval, P.; Foerster, D.; Sánchez-Portal, D. Phys. Rev. B **2014**, 89, 155417.

(12) Ke, S.-H. Phys. Rev. B **2011**, 84, 205415.

(13) Caruso, F.; Rinke, P.; Ren, X.; Rubio, A.; Scheffler, M. Phys. Rev. B **2013**, 88, 075105.

(14) Jacquemin, D.; Duchemin, I.; Blase, X. J. Chem. Theory Comput. **2015**, 11, 3290–3304.

(15) Faber, C.; Duchemin, I.; Deutsch, T.; Attaccalite, C.; Olevano, V.; Blase, X. J. Mater. Sci. **2012**, 47, 7472–7481.

(16) Neuhauser, D.; Gao, Y.; Arntsen, C.; Karshenas, C.; Rabani, E.; Baer, R. Phys. Rev. Lett. **2014**, 113, 076402.

(17) Kaplan, F.; Weigend, F.; Evers, F.; van Setten, M. J. J. Chem. Theory Comput. **2015**, 11, 5152–5160.

(18) Knight, J. W.; Wang, X.; Gallandi, L.; Dolgounitcheva, O.; Ren, X.; Ortiz, J. V.; Rinke, P.; Körzdörfer, T.; Marom, N. J. Chem. Theory Comput. **2016**, 12, 615–626.

(19) Duchemin, I.; Jacquemin, D.; Blase, X. J. Chem. Phys. **2016**, 144, 164106.

(20) Boulanger, P.; Jacquemin, D.; Duchemin, I.; Blase, X. J. Chem. Theory and Comput. **2014**, 10, 1212–1218.

(21) Bruneval, F.; Hamed, S. M.; Neaton, J. B. J. Chem. Phys. **2015**, 142, 244101.

(22) Körbel, S.; Boulanger, P.; Duchemin, I.; Blase, X.; Marques, M. A. L.; Botti, S. J. Chem. Theory Comput. **2014**, 10, 3934–3943.

(23) Blase, X.; Boulanger, P.; Bruneval, F.; Fernandez-Serra, M.; Duchemin, I. J. Chem. Phys. **2016**, 144, 034109.

(24) Jacquemin, D.; Duchemin, I.; Blase, X. Mol. Phys. **2016**, 114, 957–967.

(25) Jacquemin, D.; Duchemin, I.; Blase, X. J. Chem. Theory Comput. **2015**, 11, 5340–5359.

(26) Gonze, X. Z. Kristallogr. **2005**, 220, 558–562.

(27) Deslippe, J.; Samsonidze, G.; Strubbe, D. A.; Jain, M.; Cohen, M. L.; Louie, S. G. Comput. Phys. Commun. **2012**, 183, 1269–1289.

(28) Jiang, H.; Gómez-Abal, R. I.; Li, X.-Z.; Meisenbichler, C.; Ambrosch-Draxl, C.; Scheffler, M. Comput. Phys. Commun. **2013**, 184, 348–366.

(29) Shishkin, M.; Kresse, G. Phys. Rev. B **2006**, 74, 035101.

(30) Shishkin, M.; Kresse, G. Phys. Rev. B **2007**, 75, 235102.

(31) Shishkin, M.; Marsman, M.; Kresse, G. Phys. Rev. Lett. **2007**, 99, 246403.

(32) Fuchs, F.; Furthmüller, J.; Bechstedt, F.; Shishkin, M.; Kresse, G. Phys. Rev. B **2007**, 76, 115109.

(33) Marini, A.; Hogan, C.; Grüning, M.; Varsano, D. Comput. Phys. Commun. **2009**, 180, 1392–1403.

(34) Friedrich, C.; Blügel, S.; Schindlmayr, A. Phys. Rev. B **2010**, 81, 125102.

(35) Martin-Samos, L.; Bussi, G. Comput. Phys. Commun. **2009**, 180, 1416–1425.

(36) Umari, P.; Stenuit, G.; Baroni, S. Phys. Rev. B **2009**, 79, 201104.

(37) Usuda, M.; Hamada, N.; Kotani, T.; van Schilfgaarde, M. Phys. Rev. B **2002**, 66, 125101.

(38) Kotani, T.; van Schilfgaarde, M. Solid State Comm. **2002**, 121, 461–465.

(39) Arnaud, B.; Alouani, M. Phys. Rev. B **2000**, 62, 4464.

(40) Berger, J. A.; Reining, L.; Sottile, F. Phys. Rev. B **2012**, 85, 085126.

(41) Kutepov, A.; Haule, K.; Savrasov, S. Y.; Kotliar, G. Phys. Rev. B **2012**, 85, 155129.

(42) Hybertsen, M. S.; Louie, S. G. Phys. Rev. B **1986**, 34, 5390.

(43) Aryasetiawan, F.; Gunnarsson, O. Rep. Prog. Phys. **1998**, 61, 237–312.

(44) Onida, G.; Reining, L.; Rubio, A. Rev. Mod. Phys. **2002**, 74, 601.

(45) Hüser, F.; Olsen, T.; Thygesen, K. S. Phys. Rev. B **2013**, 87, 235132.

(46) Govoni, M.; Galli, G. J. Chem. Theory Comput. **2015**, 11, 2680–2696.

(47) Lischner, J.; Sharifzadeh, S.; Deslippe, J.; Neaton, J. B.; Louie, S. G. Phys. Rev. B **2014**, 90, 115130.

(48) Umari, P.; Stenuit, G.; Baroni, S. Phys. Rev. B **2010**, 81, 115104.

(49) van Setten, M. J.; Caruso, F.; Sharifzadeh, S.; Ren, X.; Scheffler, M.; Liu, F.; Lischner, J.; Lin, L.; Deslippe, J. R.; Louie, S. G.; Yang, C.; Weigend, F.; Neaton, J. B.; Evers, F.; Rinke, P. J. Chem. Theory Comput. **2015**, 11, 5665–5687.

(50) Lippert, G.; Hutter, J.; Parrinello, M. Mol. Phys. **1997**, 92, 477–487.

(51) The CP2K developers group, CP2K is freely available from: http://www.cp2k.org/, 2016.

(52) Hutter, J.; Iannuzzi, M.; Schiffmann, F.; VandeVondele, J. WIREs Comput. Mol. Sci. **2014**, 4, 15–25.

(53) Del Ben, M.; Hutter, J.; VandeVondele, J. J. Chem. Theory Comput. **2012**, 8, 4177–4188.

(54) Del Ben, M.; Hutter, J.; VandeVondele, J. J. Chem. Theory Comput. **2013**, 9, 2654–2671.

(55) Del Ben, M.; Schütt, O.; Wentz, T.; Messmer, P.; Hutter, J.; VandeVondele, J. Comput. Phys. Commun. **2015**, 187, 120–129.

(56) Del Ben, M.; Hutter, J.; VandeVondele, J. J. Chem. Phys. **2015**, 143, 102803.

(57) Del Ben, M.; Schönherr, M.; Hutter, J.; VandeVondele, J. J. Phys. Chem. Lett. **2013**, 4, 3753–3759.

(58) Del Ben, M.; Schönherr, M.; Hutter, J.; VandeVondele, J. J. Phys. Chem. Lett. **2014**, 5, 3066–3067.

(59) Del Ben, M.; VandeVondele, J.; Slater, B. J. Phys. Chem. Lett. **2014**, 5, 4122–4128.

(60) Marques, M. A. L.; Oliveira, M. J. T.; Burnus, T. Comput. Phys. Commun. **2012**, 183, 2272–2281.

(61) Marom, N.; Caruso, F.; Ren, X.; Hofmann, O. T.; Körzdörfer, T.; Chelikowsky, J. R.; Rubio, A.; Scheffler, M.; Rinke, P. Phys. Rev. B **2012**, 86, 245127.

(62) Atalla, V.; Yoon, M.; Caruso, F.; Rinke, P.; Scheffler, M. Phys. Rev. B **2013**, 88, 165122.

(63) Marom, N.; Ren, X.; Moussa, J. E.; Chelikowsky, J. R.; Kronik, L. Phys. Rev. B **2011**, 84, 195143.

(64) Adamo, C.; Barone, V. J. Chem. Phys. **1999**, 110, 6158.

(65) Okuno, K.; Shigeta, Y.; Kishi, R.; Miyasaka, H.; Nakano, M. J. Photochem. Photobiol. A **2012**, 235, 29.

(66) http://cccbdb.nist.gov. accessed Jun 16, 2015.

(67) Korytár, R.; Xenioti, D.; Schmitteckert, P.; Alouani, M.; Evers, F. Nat. Commun. **2014**, 5, 5000.

(68) Kivelson, S.; Chapman, O. L. Phys. Rev. B **1983**, 728, 7236.

(69) Katauro, H.; Kumazawa, Y.; Maniwa, Y.; Umezu, I.; Suzuki, S.; Ohtsuka, Y.; Achiba, Y. Synt. Met. **1999**, 103, 2555–2558.

(70) Charlier, J.-C.; Blase, X.; Roche, S. Rev. Mod. Phys. **2007**, 79, 677.

(71) Wakabayashi, K.; Fujita, M.; Ajiki, H.; Sigrist, M. Phys. Rev. B **1999**, 59, 8271.

(72) Han, M. Y.; Özyilmaz, B.; Zhang, Y.; Kim, P. Phys. Rev. Lett. **2007**, 98, 206805.

(73) Son, Y. W.; Cohen, M. L.; Louie, S. G. Phys. Rev. Lett. **2006**, 97, 216803.

(74) Wilhelm, J.; Walz, M.; Evers, F. Phys. Rev. B **2014**, 89, 195406.

(75) Castro Neto, A. H.; Guinea, F.; Peres, N. M. R.; Novoselov, K. S.; Geim, A. K. Rev. Mod. Phys. **2009**, 81, 109.

(76) Perdew, J. P.; Burke, K.; Ernzerhof, M. Phys. Rev. Lett. **1996**, 77, 3865.

(77) Plasser, F.; Pašalić, H.; Gerzabek, M. H.; Libisch, F.; Reiter, R.; Burgdörfer, J.; Müller, T.; Shepard, R.; Lischka, H. Angew. Chem. Int. Ed. **2013**, 52, 2581–2584.

(78) Hachmann, J.; Dorando, J. J.; Avilés, M.; Chan, G. K.-L. J. Chem. Phys. **2007**, 127, 134309.

(79) Bendikov, M.; Dong, H. M.; Starkey, K.; Houk, K. N.; Carter, E. A.; Wudl, F. J. Am. Chem. Soc. **2004**, 126, 7416–7417.

(80) Hajgató, B.; Szieberth, D.; Geerlings, P.; De Proft, F.; Deleuze, M. S. J. Chem. Phys. **2009**, 131, 224321.

(81) Qu, Z.; Zhang, D.; Liu, C.; Jiang, Y. J. Phys. Chem. A **2009**, 113, 7909–7914.

(82) Kadantsev, E. S.; Stott, M. J.; Rubio, A. J. Chem. Phys. **2006**, 124, 134901.

(83) Bettinger, H. F. Pure Appl. Chem. **2010**, 82, 905–915.

(84) Malloci, G.; Cappellini, G.; Mulas, G.; Mattoni, A. Chem. Phys. **2011**, 384, 19–27.

(85) Kuribara, K. et al. Nat. Commun. **2012**, 3, 723.

(86) Miao, Q.; Lefenfeld, M.; Nguyen, T.-Q.; Siegrist, T.; Kloc, C.; Nuckolls, C. Adv. Mater. **2005**, 17, 407–412.

(87) Shi, J.; Tang, C. W. Appl. Phys. Lett. **2002**, 80, 3201.

(88) Zhu, M.; Ye, T.; Li, C.-G.; Cao, X.; Zhong, C.; Ma, D.; Qin, J.; Yang, C. J. Phys. Chem. C **2011**, 115, 17965–17972.

(89) Yelin, T.; Korytár, R.; Sukenik, N.; Vardimon, R.; Kumar, B.; Nuckolls, C.; Evers, F.; Tal, O. Nat. Mater. **2016**, 15, 1476.

(90) Kippelen, B.; Bredas, J.-L. Energy Environ. Sci. **2009**, 2, 251–261.

(91) Lin, Y.; Li, Y.; Zhan, X. Chem. Soc. Rev. **2012**, 41, 4245–4272.

(92) Dissanayake, D. M. N. M.; Adikaari, A. A. D. T.; Silva, S. R. P. Appl. Phys. Lett **2008**, 92, 093308.

(93) Huang, L.; Rocca, D.; Baroni, S.; Gubbins, K. E.; Nardelli, M. B. J. Chem. Phys. **2009**, 130, 194701.

(94) Chung, D.; Park, J.; Yun, W.; Cha, H.; Kim, Y.-H.; Kwon, S.-K.; Park, C. ChemSusChem **2010**, 3, 742–748.

(95) Kohn, W.; Sham, L. J. Phys. Rev. **1965**, 140, A1133.

(96) Szabo, A.; Ostlund, N. S. Modern Quantum Chemistry; McGraw-Hill, 1989.

(97) Guidon, M.; Schiffmann, F.; Hutter, J.; VandeVondele, J. J. Chem. Phys. **2008**, 128, 214104.

(98) Guidon, M.; Hutter, J.; VandeVondele, J. J. Chem. Theory Comput. **2009**, 5, 3010–3021.

(99) Paier, J.; Diaconu, C. V.; Scuseria, G. E.; Guidon, M.; VandeVondele, J.; Hutter, J. Phys. Rev. B **2009**, 80, 174114.

(100) Whitten, J. L. J. Chem. Phys. **1973**, 58, 4496.

(101) Dunlap, B. I.; Connolly, J. W. D.; Sabin, J. R. J. Chem. Phys. **1979**, 71, 3396.

(102) Vahtras, O.; Almlöf, J.; Feyereisen, M. Chem. Phys. Lett. **1993**, 213, 514–518.

(103) Weigend, F.; Häser, M.; Patzelt, H.; Ahlrichs, R. Chem. Phys. Lett. **1998**, 294, 143–152.

(104) Hedin, L. Phys. Rev. **1965**, 139, A796.

(105) Boyd, J. P. J. Sci. Comput. **1987**, 2, 99–109.

(106) Eshuis, H.; Yarkony, J.; Furche, F. J. Chem. Phys. **2010**, 132, 234114.

(107) Rojas, H. N.; Godby, R. W.; Needs, R. J. Phys. Rev. Lett. **1995**, 74, 1827.

(108) Rieger, M. M.; Steinbeck, L.; White, I.; Rojas, H.; Godby, R. Comput. Phys. Commun. **1999**, 117, 211–228.

(109) Pham, T. A.; Nguyen, H.-V.; Rocca, D.; Galli, G. Phys. Rev. B **2013**, 87, 155148.

(110) Friedrich, C.; Betzinger, M.; Schlipf, M.; Blügel, S.; Schindlmayr, A. J. Phys. Condens. Matter **2012**, 24, 293201.

(111) VandeVondele, J.; Krack, M.; Mohamed, F.; Parrinello, M.; Chassaing, T.; Hutter, J. Comput. Phys. Commun. **2005**, 167, 103–128.

(112) VandeVondele, J.; Hutter, J. J. Chem. Phys **2003**, 118, 4365.

(113) Borštnik, U.; VandeVondele, J.; Weber, V.; Hutter, J. Parallel Comput. **2014**, 40, 47–58.

(114) Goedecker, S.; Teter, M.; Hutter, J. Phys. Rev. B **1996**, 54, 1703.

(115) Krack, M. Theor. Chem. Acc. **2005**, 114, 145–152.

(116) Vosko, S. H.; Wilk, L.; Nusair, M. Can. J. Phys. **1980**, 58, 1200–1211.

(117) Dunning, T. H. J. Chem. Phys. **1989**, 90, 1007.

(118) Woon, D. E.; Dunning, T. H. J. Chem. Phys. **1993**, 98, 1358.

(119) VandeVondele, J.; Hutter, J. J. Chem. Phys. **2007**, 127, 114105.

(120) Weigend, F.; Köhn, A.; Hättig, C. J. Chem. Phys. **2002**, 116, 3175.

(121) Genovese, L.; Deutsch, T.; Neelov, A.; Goedecker, S.; Beylkin, G. J. Chem. Phys. **2006**, 125, 074105.

(122) http://cccbdb.nist.gov/. accessed Jun 16, 2015.

(123) Guidon, M.; Hutter, J.; VandeVondele, J. J. Chem. Theory Comput. **2010**, 6, 2348–2364.

(124) Merlot, P.; Izsák, R.; Borgoo, A.; Kjærgaard, T.; Helgaker, T.; Reine, S. J. Chem. Phys. **2014**, 141, 094104.

(125) Nemeth, G.; Selzle, H.; Schlag, E. Chem. Phys. Lett. **1993**, 215, 151–155.

(126) Yanai, T.; Tew, D. P.; Handy, N. C. Chem. Phys. Lett. **2004**, 393, 51–57.

(127) Bieri, G.; Åsbrink, L.; Niessen, W. J. J. Electron. Spectrosc. Relat. Phenom. **1982**, 27, 129.

(128) Gallandi, L.; Körzdörfer, T. J. Chem. Theory Comput. **2015**, 11, 5391–5400.

(129) Krause, K.; Harding, M. E.; Klopper, W. Mol. Phys. **2015**, 113, 1952–1960.

(130) Del Ben, M.; Havenith, R. W. A.; Broer, R.; Stener, M. J. Phys. Chem. C **2011**, 115, 16782–16796.

(131) Murray, C. B.; Norris, D. J.; Bawendi, M. G. J. Am. Chem. Soc. **1993**, 115, 8706–8715.

(132) Sigalas, M. M.; Koukaras, E. N.; Zdetsis, A. D. RSC Adv. **2014**, 4, 14613–14623.

(133) Puzder, A.; Williamson, A. J.; Gygi, F.; Galli, G. Phys. Rev. Lett. **2004**, 92, 217401.

(134) Kilina, S.; Ivanov, S.; Tretiak, S. J. Am. Chem. Soc. **2009**, 131, 7717–7726.

(135) del Puerto, M. L.; Tiago, M. L.; Chelikowsky, J. R. Phys. Rev. Lett. **2006**, 97, 096401.

(136) Inerbaev, T. M.; Masunov, A. E.; Khondaker, S. I.; Dobrinescu, A.; Plamadă, A.-V.; Kawazoe, Y. J. Chem. Phys. **2009**, 131, 044106.

(137) Kuznetsov, A. E.; Beratan, D. N. J. Phys. Chem. C **2014**, 118, 7094–7109.

(138) Fischer, S. A.; Crotty, A. M.; Kilina, S. V.; Ivanov, S. A.; Tretiak, S. Nanoscale **2012**, 4, 904–914.

(139) Deglmann, P.; Ahlrichs, R.; Tsereteli, K. J. Chem. Phys. **2002**, 116, 1585.

(140) Yu, M.; Fernando, G. W.; Li, R.; Papadimitrakopoulos, F.; Shi, N.; Ramprasad, R. Appl. Phys. Lett. **2006**, 88, 231910.

(141) Kasuya, A. et al. Nat. Mater. **2004**, 3, 99.

(142) Solà, M. Front. Chem. **2013**, 1, 22.

(143) Sun, Z.; Zeng, Z.; Wu, J. Chem. Asian J. **2013**, 8, 2894–2904.

(144) Kaur, I.; Jazdzyk, M.; Stein, N. N.; Prusevich, P.; Miller, G. P. J. Am. Chem. Soc. **2010**, 132, 1261–1263.

(145) Rangel, T.; Berland, K.; Sharifzadeh, S.; Brown-Altvater, F.; Lee, K.; Hyldgaard, P.; Kronik, L.; Neaton, J. B. Phys. Rev. B **2016**, 93, 115206.

(146) Kaplan, F.; Harding, M. E.; Seiler, C.; Weigend, F.; Evers, F.; van Setten, M. J. to appear in J. Chem. Theory Comput.

(147) Rangel, T.; Hamed, S. M.; Bruneval, F.; Neaton, J. B. to appear in J. Chem. Theory. Comput.

Graphical TOC Entry